

# Synthesis and enhanced microwave-absorbing properties of SnO<sub>2</sub>/α-Fe<sub>2</sub>O<sub>3</sub>@RGO composites

Ziyao Shen<sup>1</sup> · Honglong Xing<sup>1</sup>  · Yangting Zhu<sup>1</sup> · Xiaoli Ji<sup>1</sup> · Zhenfeng Liu<sup>1</sup> · Lei Wang<sup>1</sup>

Received: 25 January 2017 / Accepted: 29 May 2017 / Published online: 1 June 2017  
© Springer Science+Business Media New York 2017

**Abstract** SnO<sub>2</sub>/α-Fe<sub>2</sub>O<sub>3</sub>@RGO composites were prepared through a solvothermal method. The phase structure, morphology, and electromagnetic (EM)-wave-absorbing properties of the as-prepared samples were characterized by X-ray diffraction, Fourier transform infrared spectroscopy, transmission electron microscopy, X-ray photoelectron spectroscopy, and vector network analyzer. Results indicated that the remarkable EM wave absorption properties of the samples resulted from the interaction between lamella-structured reduced graphene oxide and semiconductor-heterostructured SnO<sub>2</sub>/α-Fe<sub>2</sub>O<sub>3</sub>. The optical reflection loss calculated from the measured complex permittivity and permeability was -44.33 dB at 12.64 GHz. Meanwhile, the Fe<sup>3+</sup>/Sn<sup>4+</sup> molar ratio in the composites was 6:1, and the coating thickness was 2 mm. The bandwidth below -10 dB was 4.4 GHz (10.80–15.20 GHz). Therefore, SnO<sub>2</sub>/α-Fe<sub>2</sub>O<sub>3</sub>@RGO could serve as a high-performance EM-wave-absorbing material.

## 1 Introduction

Electromagnetic (EM) wave pollution has become increasingly serious due to the rapid growth of modern science technologies, and several investigators have focused their attention on EM wave absorption materials that possess a thin coating, low weight, wide frequency range, and strong absorption [1, 2]. Composite absorbing materials are expected to become a new trend in the coming years

because the practical application of traditional microwave-absorbing materials is limited by their weak absorption capability and narrow absorption band. Graphene oxide (GO), a new type of carbon material, possesses a high dielectric constant and abundant oxygen-containing groups on its surface [3]. In addition, GO is characterized by a well-developed surface area, high mechanical strength, and low weight. Given these characteristics, GO is widely used in chemical sensors [4–6], fuel cells [7, 8], catalysts [9–11], and EM-wave-absorbing materials [12–14]. Chemically reduced GO (RGO) and its composites have recently attracted the attention of researchers because of their excellent EM wave absorption properties [15, 16]. However, when RGO acts alone as an absorber, its high conductivity would worsen the impedance match and results in poor microwave absorption. The use of a composite with other materials to make the composite present multiple losses and to enhance the impedance match is an effective means to improve the microwave absorption performance. α-Fe<sub>2</sub>O<sub>3</sub> is the most stable iron oxide and an n-semiconductor; it has a band gap of 2.1 eV [17]. As a promising functional material, α-Fe<sub>2</sub>O<sub>3</sub> is always composited with RGO to synthesize the EM absorber. SnO<sub>2</sub>, which is an n-type semiconductor with a wide band gap of 3.6 eV and an excellent conductive material, has attracted considerable attention because of its diverse applications [18–21]. The addition of SnO<sub>2</sub> and α-Fe<sub>2</sub>O<sub>3</sub>, not only regulates the conductivity of RGO, but also improves impedance match and provides the composite a remarkable EM absorption performance. SnO<sub>2</sub> and α-Fe<sub>2</sub>O<sub>3</sub> have the properties of an n-type semiconductor; they can constitute semiconductor nanoheterostructures, and the effective complementarities help enhance the polarization process and promote EM wave absorbance [22, 23].

In this study, SnO<sub>2</sub>/α-Fe<sub>2</sub>O<sub>3</sub>@RGO composites were successfully synthesized through a solvothermal method.

✉ Honglong Xing  
austxhl@163.com

<sup>1</sup> School of Chemical Engineering, Anhui University of Science and Technology, Huainan 232001, China

The effects of the RGO flake and the ratio of  $\text{Fe}^{3+}/\text{Sn}^{4+}$  (2:1, 6:1, and 10:1) on microwave absorption properties were discussed. The morphology, structure, and the electromagnetic parameters of the composites were also systematically analyzed. The EM absorption measured within 2–18 GHz indicated a maximum reflection loss of  $-44.33$  dB at 12.64 GHz for the  $\text{Fe}^{3+}/\text{Sn}^{4+}$  ratio of 6:1 and coating thickness of 2 mm. The absorption band below  $-10$  dB was 4.40 GHz (10.80–15.20 GHz).

## 2 Experimental

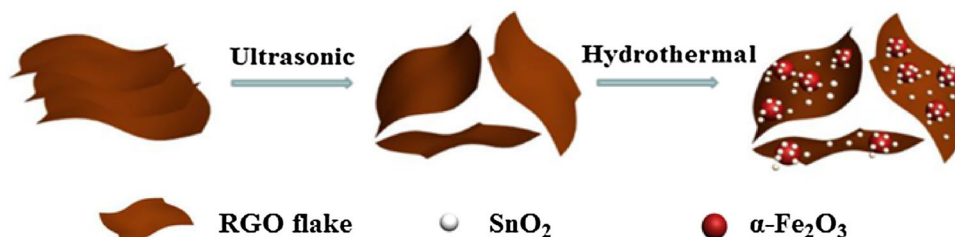
### 2.1 Materials

The natural graphite flake (25 mesh, purity of 99.9%), ammonia (purity of 25%), potassium permanganate ( $\text{KMnO}_4$ ), sodium nitrate ( $\text{NaNO}_3$ ), five hydrated stannic chlorides ( $\text{SnCl}_4 \cdot 5\text{H}_2\text{O}$ ), ferric chloride hexahydrate ( $\text{FeCl}_3 \cdot 6\text{H}_2\text{O}$ ), and other chemical reagents in this work were of analytical grade and not subjected to further purification.

### 2.2 Synthesis of $\text{SnO}_2/\alpha\text{-Fe}_2\text{O}_3$ @RGO composites

Graphene oxide (GO) flakes were synthesized from graphite powder through a modified Hummers' method [24].  $\text{SnO}_2/\alpha\text{-Fe}_2\text{O}_3$ @RGO composites were prepared through a solvothermal method. Following a typical procedure, 50 mg of GO was dispersed uniformly in 70 mL of a solution that contained 30 mL of  $\text{H}_2\text{O}$  and 40 mL of ethanol and subjected to ultrasonic dispersion for 1 h. Ferric chloride hexahydrate ( $\text{FeCl}_3 \cdot 6\text{H}_2\text{O}$ ) and five hydrated stannic chlorides ( $\text{SnCl}_4 \cdot 5\text{H}_2\text{O}$ ) were added to the solution at different molar ratios of 2:1 (S1), 6:1 (S2), and 10:1 (S3). The solution was then transferred into a 100-mL Teflon-lined stainless steel autoclave and kept at 180 °C for 12 h in an electric oven. The autoclave was cooled down to room temperature. Afterward, the obtained product was dried in a vacuum drying oven at 60 °C for 12 h. The  $\text{SnO}_2/\alpha\text{-Fe}_2\text{O}_3$ @RGO composites were then obtained. The preparation process is illustrated in Fig. 1.

**Fig. 1** Synthesis process of the  $\text{SnO}_2/\alpha\text{-Fe}_2\text{O}_3$ @RGO



### 2.3 Characterization

X-ray diffraction (XRD) using a  $\text{Cu-K}\alpha$  source ( $\lambda = 1.5481 \text{ \AA}$ ) (XRD, Beijing Purkinje General Instrument Co., Ltd.) was conducted to identify the crystal structure of the as-prepared samples. A Fourier transform infrared spectroscopy (FTIR, 170SX) was used to record the FTIR spectra of the samples over the range of  $400\text{--}4000 \text{ cm}^{-1}$ . The morphologies of the samples were observed with a transmission electron microscope (TEM, FEI Tecnai 12) with an acceleration voltage of 200 kV. The surface composition was obtained through X-ray photoelectron spectroscopy (XPS, ESCALAB210). The complex permittivity ( $\epsilon_r$ ) and complex permeability ( $\mu_r$ ) of the samples (uniformly mixing 60 wt.%  $\text{SnO}_2/\alpha\text{-Fe}_2\text{O}_3$ @RGO composites with paraffin and pressing the mixture into a toroid mold with an outer diameter of 7.0 mm and an inner diameter of 3.04 mm) were measured in a frequency range of 2–18 GHz by using a vector network analyzer (AV3629D) at room temperature.

## 3 Results and discussion

Figure 2a presents the XRD pattern of the  $\text{SnO}_2/\alpha\text{-Fe}_2\text{O}_3$ @RGO composites (S1, S2, and S3). The RGO diffraction peaks cannot be observed in Fig. 2a because the ordered structure of the natural graphite flake was damaged in the GO preparation process, and reassembly of GO was prevented by the development of  $\text{SnO}_2$  and  $\alpha\text{-Fe}_2\text{O}_3$  on the RGO surface in the solvothermal process. The relative intensities of the diffraction peaks at  $2\theta = 24.14^\circ, 33.14^\circ, 35.61^\circ, 40.84^\circ, 49.43^\circ, 54.02^\circ, 57.57^\circ, 62.40^\circ, 63.97^\circ, 71.85^\circ, 75.37^\circ$  are assigned to the reflections from the (012), (104), (110), (113), (024), (116), (018), (214), (300), (1010), and (220) planes of  $\alpha\text{-Fe}_2\text{O}_3$  (JCPDS card No. 33-0664), respectively. For  $\text{SnO}_2$ , three peaks at  $26.60^\circ, 33.85^\circ, \text{ and } 51.76^\circ$  were observed and could be indexed as characteristic (110), (101), and (211) reflections, respectively, of the  $\text{SnO}_2$  crystal (JCPDS card No. 41-1445). These results suggest the existence of  $\text{SnO}_2$  and  $\alpha\text{-Fe}_2\text{O}_3$  [25, 26]. No other impure phases were detected. Notably, no obvious diffraction peaks for RGO can be observed in  $\text{SnO}_2/\alpha\text{-Fe}_2\text{O}_3$ @RGO composites, which might be the relative low diffraction intensity of RGO in the composite of

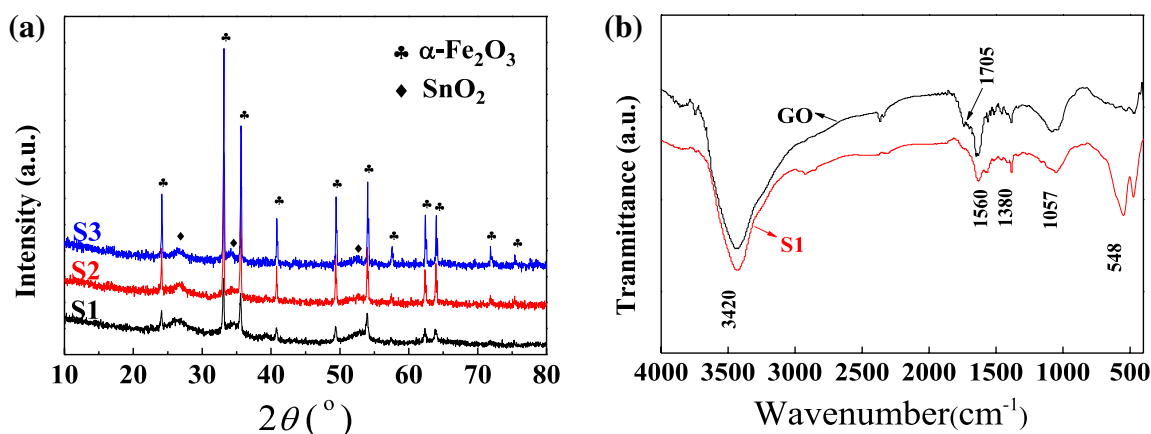


**Fig. 2** XRD pattern of S1, S2, and S3 and FTIR spectra of GO and S1

the SnO<sub>2</sub>/α-Fe<sub>2</sub>O<sub>3</sub>@RGO composites compared with SnO<sub>2</sub> and α-Fe<sub>2</sub>O<sub>3</sub> nanoparticles [27].

The FTIR spectra of GO and SnO<sub>2</sub>/α-Fe<sub>2</sub>O<sub>3</sub>@RGO composites (S1) are shown in Fig. 2b. The peak at 3420 cm<sup>-1</sup> is assigned to the O–H deformation vibration in graphene and intercalated water in the samples [28]. The peak at 1705 cm<sup>-1</sup> is attributed to the C=O stretching of carbonyl and carboxyl groups at the edges of the GO networks. The peaks at 1380 and 1057 cm<sup>-1</sup> are due to –CH<sub>3</sub> deformation vibrations and C–O stretching vibration, respectively [29, 30]. Comparison of the FTIR spectrum of GO with that of S1 revealed that the peaks at 1705 and 1057 cm<sup>-1</sup> weakened in S1, indicating that GO was reduced in the preparation of SnO<sub>2</sub>/α-Fe<sub>2</sub>O<sub>3</sub>@RGO composites. The peak at 1560 cm<sup>-1</sup> is associated with the formation of –COO after RGO was coated with SnO<sub>2</sub> and α-Fe<sub>2</sub>O<sub>3</sub>. The broad peak at 548 cm<sup>-1</sup> corresponds to Fe–O and Sn–O vibration.

To further determine the chemical composition of the SnO<sub>2</sub>/α-Fe<sub>2</sub>O<sub>3</sub>@RGO composites, Fig. 3 shows the XPS spectra of S1. Figure 3a presents the full-scan XPS spectra of S1 and indicates that the elements on the surface of S1 were Fe, C, O, and Sn. The C1s spectra (Fig. 3b) revealed four types of carbon bonds at 284.7 eV (C–C), 285.6 eV (C–O), 286.7 eV (C=O), and 288.8 eV (O–C=O) [31]. The intensities of C–O, C=O, and O–C=O were much weaker than that of C–C, which suggests a reduction in GO. Figure 3c provides the O1s XPS spectra. The banding energy peaks at 530.3, 530.5, 530.9, 531.6, and 532.8 eV represent Fe–O, Sn–O, C=O, O–H, and C–O, respectively [27]. The energy peaks at 711.4 and 725.4 eV in the Fe 2p XPS spectra (Fig. 3d) agreed well with those in Fe 2p<sub>3/2</sub> and Fe 2p<sub>1/2</sub>. The binding energy peaks at approximately 716.3 and 732.7 eV that accompanied Fe 2p<sub>3/2</sub> and Fe 2p<sub>1/2</sub> are characteristics of γ-Fe<sub>2</sub>O<sub>3</sub>. The two peaks at 486.8 and 459.2 eV are assigned to Sn 3d<sub>5/2</sub> and Sn 3d<sub>3/2</sub>, respectively [32].

The morphology of composites is characterized by SEM and TEM, Fig. 4 shows the results. From Fig. 4a, it's obvious that the GO flake was fabricated successfully. Figure 4b shows that the nanoparticles were well loaded on the surface of GO flake. A thin-layered structure RGO with some wrinkles can be observed in the Fig. 4c, d. And it also can be seen from the images that there are two sizes of particles well scattered on the RGO, only a small fraction dispersed in the solution. HRTEM image of composites from the surface of RGO (inset of Fig. 4d) show two different clear lattice fringes. The crystal lattice spacing of the bigger particles is 0.27 nm (Fig. 4e) can be assigned to the (104) plane of α-Fe<sub>2</sub>O<sub>3</sub> particles, while the lattice of the smaller particles is 0.35 nm (Fig. 4f), corresponding to the (110) plane of SnO<sub>2</sub> particles. The results are consistent with the XRD pattern. Therefore, we can identify the nanoparticles with range of 5–10 nm in the Fig. 4d are SnO<sub>2</sub> nanoparticles, and α-Fe<sub>2</sub>O<sub>3</sub> have a larger particles size around 25 nm.

Transmission coaxial line theory states that complex permittivity ( $\epsilon_r = \epsilon' - j\epsilon''$ ), complex permeability ( $\mu_r = \mu' - j\mu''$ ), coating thickness ( $d$ ), and frequency ( $f$ ) are the main factors that affect the absorption performance of samples. We studied the EM parameters of the sample-paraffin mixture at the frequency of 2–18 GHz at room temperature to obtain additional EM absorption properties of the samples. Figure 5a shows that the real part of the relative permittivity ( $\epsilon'$ ) of the three samples exhibited a downward trend. The  $\epsilon'$  of S2 was larger than those of the other two samples in the entire testing frequency range. Figure 5b indicates that the imaginary part of the relative permittivity ( $\epsilon''$ ) of S3 exhibited a distinct decrease, whereas the  $\epsilon''$  of S2 and S3 almost remained unchanged from 2 to 14 GHz and then exhibited some fluctuation at increased frequency. In the beginning of 6 GHz, the  $\epsilon''$  values of S2 exceeded those of S3 and became the largest among the three samples. The increased value of  $\epsilon'$  might be due to

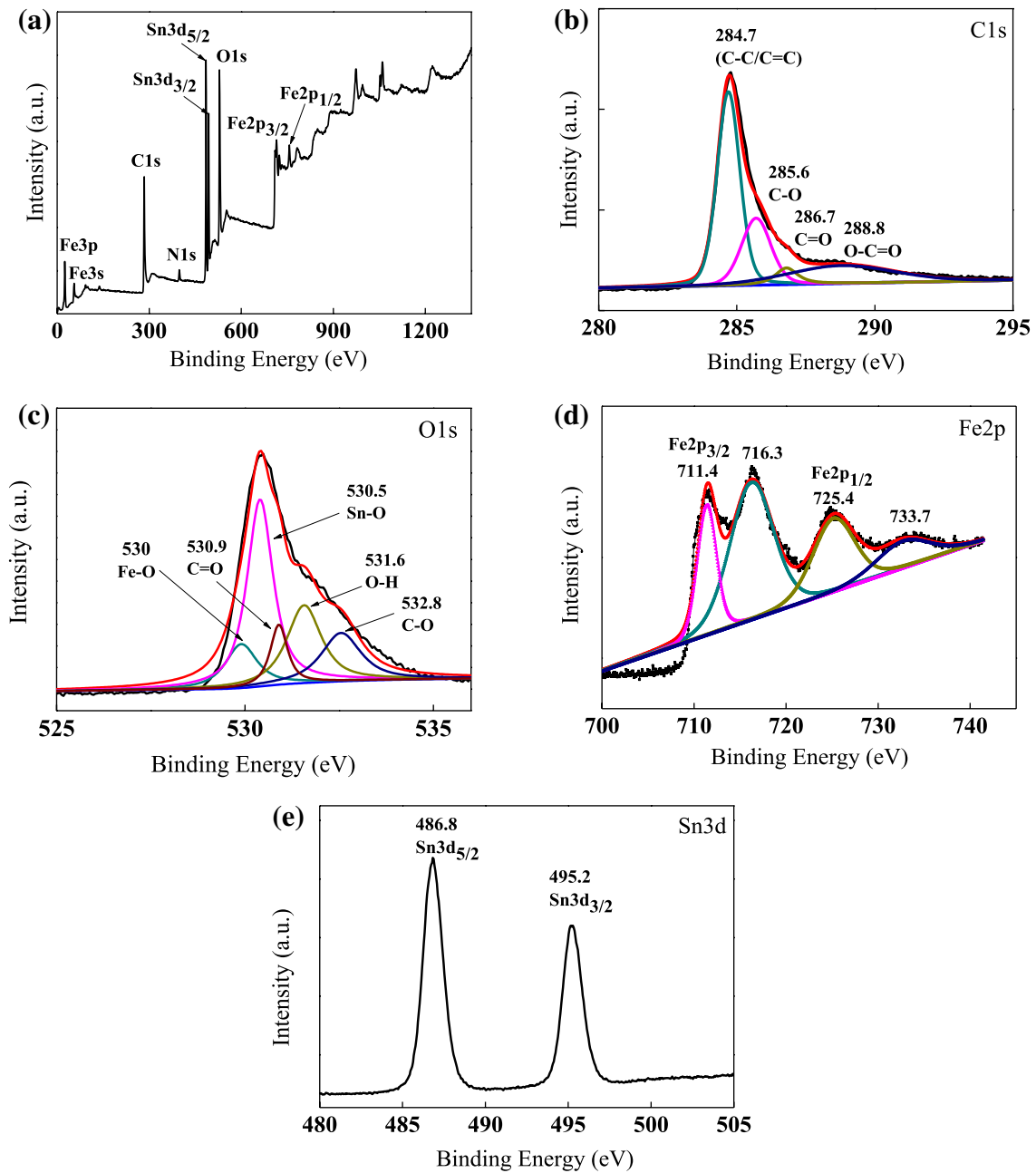
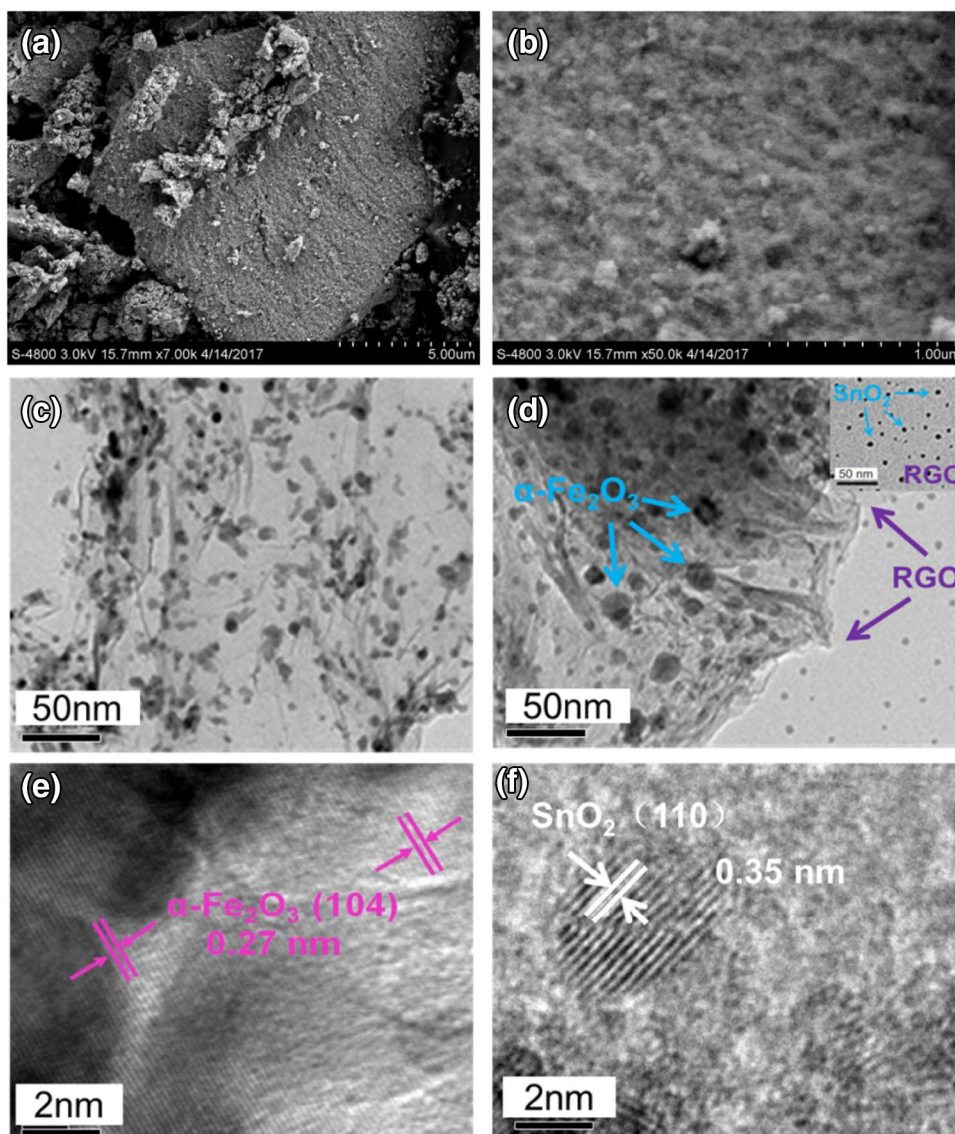


**Fig. 3** XPS spectra of S1: **a** wide span, **b** C1s spectrum, **c** O1s spectrum, **d** Fe2p spectrum, and **e** Sn3d spectrum

the enhancement of interfacial polarization [1]. The multi-interface between the RGO layer and SnO<sub>2</sub>/α-Fe<sub>2</sub>O<sub>3</sub> and the proper Fe<sup>3+</sup>/Sn<sup>4+</sup> molar ratio promoted the polarization process. Free electron theory posits that  $\epsilon'' = \sigma / (2\pi f \epsilon_0)$  [33], where  $\sigma$  is the electrical conductivity; thus, the  $\epsilon''$  values of the composites at 2–18 GHz represent the electrical conductivities. The higher  $\epsilon''$  value of S3 from 2 to 6 GHz indicate high conductivity, and the same applies to S2 from 6 to 18 GHz. Therefore, an enhanced dielectric loss could be achieved by changing the Fe<sup>3+</sup>/Sn<sup>4+</sup> molar ratio.

Figure 5c shows that the real part of the permeability ( $\mu'$ ) of S1 decreased with slight undulation and exhibited the same tendency as S2 and S3. Figure 5d shows that the imaginary part of the permeability ( $\mu''$ ) of the three samples had two resonance peaks at a low frequency, whereas the peaks were not distinct with increased frequency. Under the coaction of RGO and SnO<sub>2</sub>/α-Fe<sub>2</sub>O<sub>3</sub> nanoparticles, the values of  $\mu'$  and  $\mu''$  remained stable at 0.98–1.20 and –0.017–0.21, respectively. With the change in the Fe<sup>3+</sup>/Sn<sup>4+</sup> molar ratio, the magnetic loss property of the

**Fig. 4** SEM images (a and b), TEM images (c and d) and HRTEM images (e and f) of S1



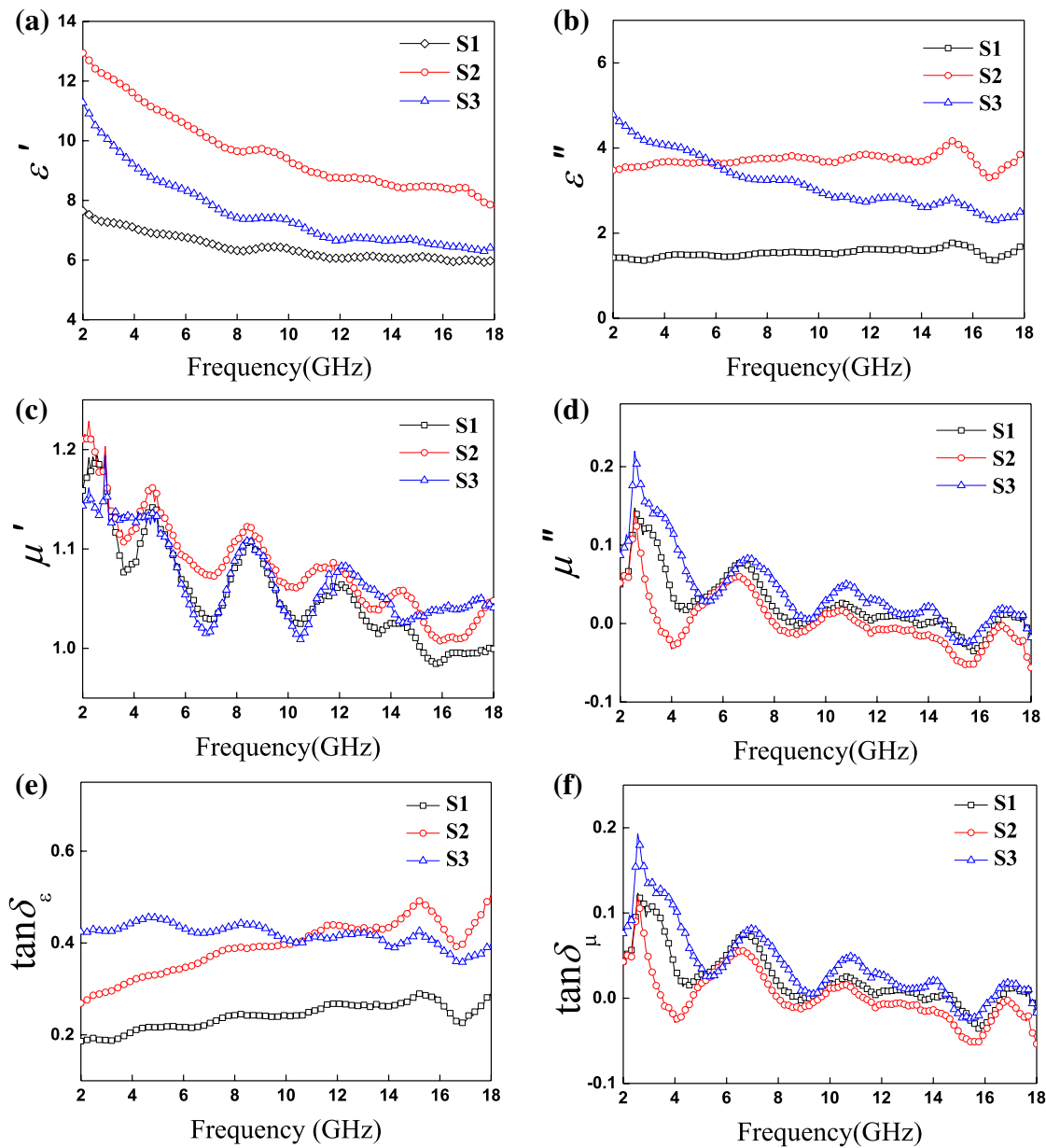
composites improved and was thus more competent in dissipating magnetic energy [34].

Figure 5e, f show the dielectric loss tangent ( $\tan\delta_e$ ) and magnetic loss tangent ( $\tan\delta_\mu$ ) of  $\text{SnO}_2/\alpha\text{-Fe}_2\text{O}_3/\text{RGO}$ -paraffin composites. The flaws of the nanoparticles (vacancy, hanging key, etc.) were easy to be polarized and subsequently generated a dielectric loss in the process of new polarization under the influence of EM wave. Figure 5e shows that the  $\tan\delta_e$  values of the three samples changed to above 0.18, which indicates that the dielectric loss existed in the entire frequency range and proved the obvious dielectric loss capability of RGO,  $\text{SnO}_2$ , and  $\alpha\text{-Fe}_2\text{O}_3$ . The  $\tan\delta_e$  of S2 was higher from 2 to 10.4 GHz. When the frequency increased, the  $\tan\delta_e$  of S3 became the highest. The  $\tan\delta_\mu$  curves of the three samples in Fig. 5f fluctuate within a narrow range at approximately 0. All of the samples had higher  $\tan\delta_e$  values than  $\tan\delta_\mu$  in 2–18 GHz, which

reveals that the dielectric loss mainly contributed to EM absorption.

The microwave absorption properties of absorbers have a close connection with impedance match. The synergistic effect of dielectric and magnetic losses makes composites satisfy material impedance matching, thereby promoting the microwave-absorbing performance. Dipole polarization in  $\alpha\text{-Fe}_2\text{O}_3$  and  $\alpha\text{-Fe}_2\text{O}_3$  at the nanoscale could enhance the polarization capability [35]. In the ternary composites, electronic and ionic polarizations caused by electron transfer among  $\text{Fe}^{3+}$ ,  $\text{Sn}^{4+}$ , and RGO also occur.

The multi-interfaces among  $\text{SnO}_2/\alpha\text{-Fe}_2\text{O}_3$ ,  $\text{SnO}_2/\alpha\text{-Fe}_2\text{O}_3/\text{RGO}$ , and  $\alpha\text{-Fe}_2\text{O}_3/\text{RGO}$  could induce more interfacial polarization and corresponding relaxations, which led to enhanced microwave attenuation ability [36]. Specially, as their similar properties of n-type semiconductor,  $\text{SnO}_2$  and  $\alpha\text{-Fe}_2\text{O}_3$  will constitute semiconductor



**Fig. 5** Real and imaginary parts of permittivity (**a**  $\epsilon'$  and **b**  $\epsilon''$ ), permeability (**c**  $\mu'$  and **d**  $\mu''$ ), and loss tangent: **e** dielectric loss tangent; **f** magnetic loss tangent of S1, S2, and S3

nanoheterostructures in the composites, and the interfacial polarization could happen in the heterogeneous system [37, 38]. Therefore, the desirable performance in microwave absorbing could be ascribed to the unique interfacial interaction of the binary components [22].

We used the Debye dipolar relaxation model [39, 40] (Cole–Cole model) to explain further the mechanism of dielectric loss. Relative complex permittivity  $\epsilon_r$  can be described as follows [41]:

$$\epsilon_r = \epsilon_\infty + \frac{\epsilon_s - \epsilon_\infty}{1 + j2\pi f\tau}, \tag{1}$$

where  $f$  is the frequency;  $\tau$  is the polarization time; and  $\epsilon_s$  and  $\epsilon_\infty$  are the static dielectric constant and the optical dielectric constant at the infinite frequency, respectively. Equation (1) shows that

$$\epsilon' = \epsilon_\infty + \frac{\epsilon_s - \epsilon_\infty}{1 + (2\pi f)^2\tau^2}, \tag{2}$$

$$\epsilon'' = \frac{2\pi f\tau(\epsilon_s - \epsilon_\infty)}{1 + (2\pi f)^2\tau^2}. \tag{3}$$

The above equations show that the relationship between  $\epsilon'$  and  $\epsilon''$  could be deduced as

$$(\epsilon' - \epsilon_\infty)^2 + (\epsilon'')^2 = (\epsilon_s - \epsilon_\infty). \quad (4)$$

Therefore, from graph  $\epsilon''$  according to  $\epsilon'$ , we can generate a semicircle that is usually defined as a Cole–Cole semicircle, and each semicircle corresponds to a type of Debye relaxation process [42]. Figure 6a–c display the Cole–Cole vibration curves of the as-prepared samples. Two semicircles of the curves are shown in Fig. 6a, c. Hence, S1 and S3 had two types of Debye relaxation at the least. Figure 6b shows that the number of semicircles for S2 is three. The increase in the Debye process implied that the S2 composite had more enhanced dielectric properties.

Microwave absorption properties were investigated by mixing 60 wt% of the samples with paraffin. From the obtained EM parameters, the reflection loss (RL) of S1, S2, and S3 was calculated according to transmission theory by using the following equations [43, 44].

$$Z_{in} = \sqrt{\frac{\mu_r}{\epsilon_r}} \tanh \left[ j \left( \frac{2\pi df}{c} \right) \sqrt{\mu_r \epsilon_r} \right], \quad (5)$$

$$RL(\text{dB}) = 20 \lg \left| \frac{Z_{in} - Z_0}{Z_{in} + Z_0} \right|, \quad (6)$$

where  $Z_{in}$  is the input impedance of the absorber,  $Z_0$  is the impedance of free space,  $\mu_r$  is complex permeability,  $\epsilon_r$  is complex permittivity,  $f$  is the frequency of microwaves,  $d$  is the thickness of the absorber, and  $c$  is the velocity of EM waves in free space. The absorber achieved 90% microwave absorption when the RL values of the sample reached  $-10$  dB [45].

The RL of the three samples with different thicknesses is shown in Fig. 7. The RL curves of the samples presented different variation trends with different  $\text{Fe}^{3+}/\text{Sn}^{4+}$

molar ratios. For S1, the minimum RL values shifted to a low frequency when the thickness was increased. The optimal RL of S1 was  $-12.14$  dB with a thickness of 4.5 mm at 6.72 GHz, and the bandwidth below  $-10$  dB was 1.12 GHz (6.16–7.28 GHz). Figure 7b shows that the minimum RL of S2 reached  $-44.33$  dB with a thickness of 2 mm at 12.64 GHz, and the bandwidth below  $-10$  dB was 4.40 GHz (10.80–15.20 GHz). When the  $\text{Fe}^{3+}/\text{Sn}^{4+}$  ratio increased to 10:1, the minimum RL was  $-33.42$  dB with a thickness of 3.5 mm at 7.76 GHz, and the bandwidth below  $-10$  dB was 2.72 GHz (6.56–9.28 GHz). S2 possessed better EM-absorbing properties than the other two samples. The promotion of EM absorption performance can be explained by the following facts. Firstly, the addition of  $\text{SnO}_2/\alpha\text{-Fe}_2\text{O}_3$  to RGO led to interfacial and electric polarization. Secondly, the residual defects and groups in RGO with lamellar structure can act as polarized centers, which are favorable for the EM wave attenuation [46]. With an increase in frequency, the minimum value of the  $\text{SnO}_2/\alpha\text{-Fe}_2\text{O}_3$ @RGO composites corresponding to different matching thicknesses moved to a reduced frequency mainly because the increasing thickness of the absorber multiplied the wavelength of the EM waves that could interfere with one another; the corresponding frequency decreased. The result could be explained by the following equations [47].

$$d = n\lambda_m/4 (n = 1, 3, 5, 7, 9, \dots), \quad (7)$$

$$\lambda_m = \frac{c}{f \sqrt{|\epsilon_r| |\mu_r|}}, \quad (8)$$

where  $\epsilon_r$  and  $\mu_r$  are the complex relative permittivity and permeability of the absorber, respectively. The aforementioned equations indicate that the matching thickness increased with decreasing frequency. Figure 7 also reveals that all of the three  $\text{SnO}_2/\alpha\text{-Fe}_2\text{O}_3$ @RGO composite samples could complete absorption over the range of

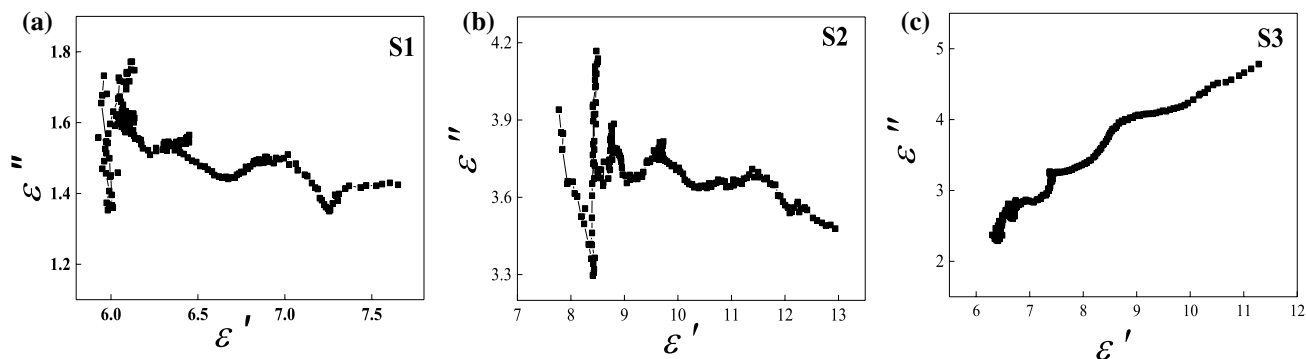


**Fig. 6** Typical Cole–Cole semicircles for  $\text{SnO}_2/\alpha\text{-Fe}_2\text{O}_3$ @RGO (S1, S2, and S3) composites

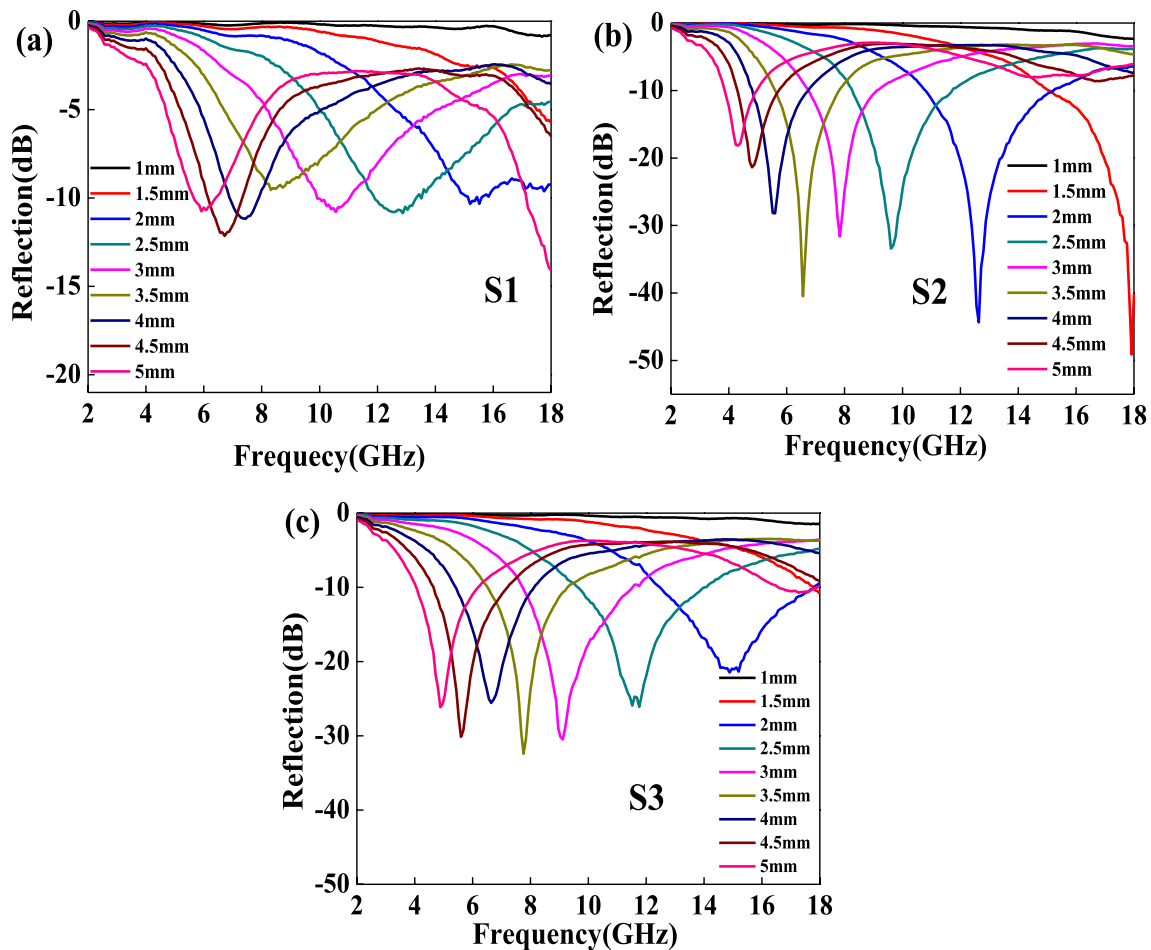


**Fig. 7** Frequency dependence of the RL values of the  $\text{SnO}_2/\alpha\text{-Fe}_2\text{O}_3/\text{RGO}$  composites (S1, S2, and S3)

4–18 GHz with 90% absorptivity and a wide bandwidth. The good absorbing performance of the  $\text{SnO}_2/\alpha\text{-Fe}_2\text{O}_3/\text{RGO}$  composites could be explained by the excellent interfacial and dipole polarization. When the  $\text{Fe}^{3+}/\text{Sn}^{4+}$  molar ratio reached 6:1, the composites exhibited superior performance. The enhanced microwave absorption properties of S2 may be attributed to the proper ratio positively affecting the properties of  $\text{SnO}_2/\alpha\text{-Fe}_2\text{O}_3$  nanoparticles and meeting the demands of impedance matching and attenuation.

## 4 Conclusions

A series of  $\text{SnO}_2/\alpha\text{-Fe}_2\text{O}_3/\text{RGO}$  composites with different  $\text{Fe}^{3+}/\text{Sn}^{4+}$  molar ratios was successfully prepared through a solvent–thermal method. In the ternary composite,  $\text{SnO}_2/\alpha\text{-Fe}_2\text{O}_3$  nanoparticles were uniformly distributed on the surface of lamellar RGO, which led to interfacial and dipole polarization. The heterostructure between  $\text{SnO}_2$  and  $\alpha\text{-Fe}_2\text{O}_3$  improved the EM wave attenuation of the absorber by promoting the polarization process. All three samples

achieved effective absorption in the measuring frequency scale. The EM wave absorption of the as-prepared composites could be optimized by setting the  $\text{Fe}^{3+}/\text{Sn}^{4+}$  molar ratio to 6:1. The minimum RL was  $-44.33$  dB at 12.64 GHz with a thickness of 2 mm, and the bandwidth below  $-10$  dB was 4.40 GHz (10.80–15.20 GHz).  $\text{SnO}_2/\alpha\text{-Fe}_2\text{O}_3/\text{RGO}$  composites are therefore promising potential absorbers with high performance.

**Acknowledgements** This work was supported by the National Natural Science Foundation of China (Grant 51477002), and the Graduate Innovation Fund Project of Anhui University of Science and Technology.

## References

1. H.Y. Wang, D.M. Zhu, W.C. Zhou, F. Luo, J. Magn. Mater. **393**, 445–451 (2015)
2. H. Qin, Q.L. Liao, G.J. Zhang, Y.H. Huang, Y. Zhang, Appl. Surf. Sci. **286**, 7–11 (2013)
3. X. Zhao, Y.L. Zhang, X.X. Wang, H.L. Shi, W.Z. Wang, M.S. Cao, J. Mater. Sci. **27**, 11518–11523 (2016)



4. F. Schedin, A.K. Geim, S.V. Morozov, E.W. Hill, P. Blake, M.I. Katsnelson, K.S. Novoselov, *Nat. Mater.* **6**, 652–655 (2007)
5. S. Mao, G.H. Lu, J.H. Chen, *J. Mater. Chem. A* **2**, 5573–5579 (2014)
6. H. Zhang, A.J. Xie, Y.H. Shen, L.G. Qiu, X.Y. Tian, *Phys. Chem. Chem. Phys.* **14**, 12757–12763 (2012)
7. Y.H. Li, L. Han, B.G. An, Y.Y. Wang, L. Wang, X.T. Yin, J.L. Lu, *J. Mater. Sci.* **27**, 6208–6215 (2016)
8. M.M. Liu, R.Z. Zhang, W. Chen, *Chem. Rev.* **114**, 5117–5160 (2014)
9. T. Xue, S. Jiang, Y.Q. Qu, Q. Su, R. Cheng, S. Dubin, C.Y. Chiu, R. Kaner, Y. Huang, X.F. Duan, *Angew. Chem.* **124**, 3888–3891 (2012)
10. C.Y. He, J.J. Zhang, P.K. Shen, *J. Mater. Chem. A* **2**, 3231–3236 (2014)
11. Z.H. Sheng, H.L. Gao, W.J. Bao, F.B. Wang, X.H. Xia, *J. Mater. Chem.* **22**, 390–395 (2012)
12. Q. Yin, H.L. Xing, R.W. Shu, X.L. Ji, D.X. Tan, Y. Gan, *Nano* **11**, 1650058 (2016)
13. V.K. Singh, A. Shukla, M.K. Patra, L. Saini, R.J. Jani, S.R. Vadera, N. Kummur, *Carbon* **50**, 2202–2208 (2012)
14. Y. Zhang, Y. Huang, T.F. Zhang, H.C. Chang, P.S. Xiao, H.H. Chen, Z.Y. Huang, Y.S. Chen, *Adv. Mater.* **27**, 2049–2053 (2015)
15. F.B. Meng, W. Wei, J.J. Chen, X.N. Chen, X.L. Xu, M. Jiang, Y. Wang, J. Lu, Z.W. Zhou, *RSC Adv.* **5**, 101121–101126 (2015)
16. T.H. Wang, Y.F. Li, L.N. Wang, C. Liu, S. Geng, X.L. Jia, F. Yang, L.Q. Zhang, L.P. Liu, B. You, X.R. Ren, H.T. Yang, *RSC Adv.* **5**, 60114–60120 (2015)
17. M. Kosa, H.N. Barad, V. Singh, D.A. Keller, K. Shimanovich, S. Rühle, A.Y. Anderson, A. Zaban, D.T. Major, *Phys. Chem. Chem. Phys.* **18**, 781–791 (2016)
18. L. Lin, H.L. Xing, R.W. Shu, L. Wang, X.L. Ji, D.X. Tan, Y. Gan, *RSC Adv.* **5**, 94539–94550 (2015)
19. X.S. Zhou, L.J. Wan, Y.G. Guo, *Adv. Mater.* **25**, 2152–2157 (2013)
20. S. Kumar, R. Nigam, V. Kundu, N. Jaggi, *J. Mater. Sci.* **26**, 3268–3274 (2015)
21. K. Kravchuk, L. Protesescu, M.I. Bodnarchuk, F. Krumeich, M. Yarema, M. Walter, C. Guntlin, M.V. Kovalenko, *J. Am. Chem. Soc.* **135**, 4199–4202 (2013)
22. C.S. Biju, D.H. Raja, D.P. Padiyan, *Chem. Phys. Lett.* **619**, 1–6 (2015)
23. Y.J. Chen, P. Gao, R.X. Wang, C.L. Zhu, L.J. Wang, M.S. Cao, H.B. Jin, *J. Phys. Chem. C* **113**, 10061–10064 (2009)
24. D.C. Marcano, D.V. Kosynkin, J.M. Berlin, A. Sinitskii, Z.Z. Sun, A. Slesarev, L.B. Alemany, W. Liu, J.M. Tour, *ACS Nano* **4**, 4806–4814 (2010)
25. L.W. Jia, J.L. Xie, C.X. Guo, C.M. Li, *RSC Adv.* **5**, 62611–62618 (2015)
26. L.F. Da Silva, O.F. Lopes, A.C. Catto, W. Avansi Jr., M.I.B. Bernardi, M.S. Li, C. Ribeiro, E. Longo, *RSC Adv.* **6**, 2112–2118 (2016)
27. H. Zhang, A.J. Xie, C.P. Wang, H.S. Wang, Y.H. Shen, X.Y. Tian, *J. Mater. Chem. A* **1**, 8547–8552 (2013)
28. M.H. Tan, G.H. Yang, T.J. Wang, T. Vitidsant, J. Li, Q.H. Wei, P.P. Ai, M.B. Wu, J.T. Zheng, N. Tsubaki, *Catal. Sci. Technol.* **6**, 1162–1172 (2016)
29. B. Gryb, S. Gryglewicz, A. Sliwak, N. Dzię, J. Machnikowski, G. Gryglewicz, *RSC Adv.* **6**, 15782–15787 (2016)
30. M. Khandelwal, A. Kumar, *Dalton Trans.* **45**, 5180–5195 (2016)
31. K.L. Zhang, Y.H. Xu, Y. Lu, Y.C. Zhu, Y.Y. Qian, D.F. Wang, J.B. Zhou, N. Lin, Y.T. Qian, *J. Mater. Chem. A* **4**, 6404–6410 (2016)
32. M. Madian, M. Klose, T. Jaumann, A. Gebert, S. Oswald, N. Ismail, A. Eychmüller, J. Eckert, L. Giebeler, *J. Mater. Chem. A* **4**, 5542–5552 (2016)
33. B.T. Draine, P.J. Flatau, *JOSA A*, **11**, 1491–1499 (1994)
34. H.B. Zhao, Z.B. Fu, H.B. Chen, M.L. Zhong, C.Y. Wang, *ACS Appl. Mater. Interfaces* **8**, 1468–1477 (2016)
35. N. Iordanova, M. Dupuis, K.M. Rosso, *J. Chem. Phys.* **122**, 144305 (2005)
36. B. Zhao, B.B. Fan, Y.W. Xu, G. Shao, X.D. Wang, W.Y. Zhao, R. Zhang, *ACS Appl. Mater. Interfaces* **7**, 26217–26225 (2015)
37. Y.Y. Lü, Y.T. Wang, H.L. Li, Y. Lin, Z.Y. Jiang, Z.X. Xie, Q. Kuang, L.S. Zheng, *ACS Appl. Mater. Interfaces* **7**, 13604–13611 (2015)
38. X.F. Zhang, P.F. Guan, X.L. Dong, *Appl. Phys. Lett.* **96**, 223111 (2010)
39. P.J. Liu, Z.J. Yao, J.T. Zhou, Z.H. Yang, L.B. Kong, *J. Mater. Chem. C* **4**, 9738–9749 (2016)
40. P. Toneguzzo, O. Acher, G. Viau, F. Fiévet-Vincent, F. Fiévet, *J. Appl. Phys.* **81**, 5546–5548 (1997)
41. J. Frenkel, J. Dorfman, *Nature* **126**, 274–275 (1930)
42. P.H. Fang, *J. Chem. Phys.* **42**, 3411–3413 (1965)
43. Y. Naito, K. Suetake, *IEEE Trans. Microw. Theory Tech.* **19**, 65–72 (1971)
44. S.S. Kim, S.B. Jo, K.I. Gueon, K.K. Choi, J.M. Kim, K.S. Churn, *IEEE Trans. Magn.* **27**, 5462–5464 (1991)
45. L.G. Yan, J.B. Wang, X.H. Han, Y. Ren, Q.F. Liu, F.S. Li, *Nanotechnology* **21**, 095708 (2010)
46. M. Zong, Y. Huang, Y. Zhao, X. Sun, C.H. Qu, D.D. Luo, J.B. Zheng, *RSC Adv.* **3**, 23638–23648 (2013)
47. A.N. Yusoff, M.H. Abdullah, S.H. Ahmad, S.F. Jusoh, A.A. Mansor, A.A. Hamid, *J. Appl. Phys.* **92**, 876–882 (2002)